

Reactive infiltration of hydrous melt above the mantle transition zone

Garrett M. Leahy^{1,2} and David Bercovici¹

Received 3 July 2009; revised 7 January 2010; accepted 16 March 2010; published 14 August 2010.

[1] Seismic studies repeatedly image a low-velocity layer overlying the mantle transition zone in tectonic settings ranging from subduction zones to continental cratons. This layer has been hypothesized to result from the presence of a dense partial melt formed by dehydration melting as relatively wet transition zone material is advected by convection currents into the low-water-solubility upper mantle. Here we examine this hypothesis by considering the dynamic infiltration of a low-viscosity reactive hydrous melt into a high-viscosity ambient solid. The thickness of the melt layer is strongly controlled by return flow induced in the surrounding viscous solid, and in steady state a dynamic equilibrium is achieved where the melt lens is restrained from collapse by the exterior mantle. Melt layers with thicknesses in excess of 10 km develop for a wide range of mantle parameters and develop on timescales equivalent to the lifespan of an ocean basin.

Citation: Leahy, G. M., and D. Bercovici (2010), Reactive infiltration of hydrous melt above the mantle transition zone, *J. Geophys. Res.*, 115, B08406, doi:10.1029/2009JB006757.

1. Introduction

[2] The “transition zone water filter” (TZWF) model [Bercovici and Karato, 2003; Karato *et al.*, 2006] stipulates that the melting of upwelling mantle and the accumulation of a dense, hydrous melt above the 410-km mantle discontinuity may explain chemical differences between mid-ocean ridge basalts and ocean island basalts while maintaining whole mantle convection. The model relies on a large difference in solidus water concentration between wadsleyite in the transition zone and olivine in the upper mantle [Inoue, 1994; Ohtani *et al.*, 2000]. As slightly wet wadsleyite (with high water storage capacity) is advected above the 410-km discontinuity and transforms to olivine (with low water storage capacity) partial melting ensues, stripping the residual solid mantle of its incompatible trace elements. A key part of this hypothesis is that water and other incompatible elements must eventually return to the lower mantle, in order to preserve the differences in the upper and lower mantle chemical reservoirs over long timescales.

[3] While the exact petrological conditions for melting and the physical properties of the melt remain areas of active research [Hirschmann *et al.*, 2005], many recent seismological studies claim to image melt above the transition zone in a variety of tectonic environments [e.g., Vinnik and Farra, 2002; Song *et al.*, 2004; Fee and Dueker, 2004; Gao *et al.*, 2004, 2006; Courtier and Revenaugh, 2007; Jasbinsek and

Dueker, 2007; Leahy, 2009]. These studies have used a variety of techniques (teleseismic receiver functions, ScS reverberations, and waveform fitting) to demonstrate the need for a low seismic velocity layer directly above the 410 km discontinuity. Estimates of thickness have ranged from 20 to 50+ km. Additionally, estimates of water concentration in the transition zone indicate that there may be enough water to cause melting [Huang *et al.*, 2005; Medin *et al.*, 2007]. These observations necessitate the development of theoretical models for melt layer structure by which the TZWF model can be tested.

[4] Bercovici and Karato [2003] proposed a mechanism for water and melt recycling by slab entrainment. In their model, silicates crystallize from the melt near the slab, and in conjunction with diffusion of water into the slab, this returns water to the transition zone. Because the magnitude of water loss to the slab depends on the melt slab contact area, the melt layer thickens until a steady state cycle of water and silicates is achieved. This model neglects how melt spreads in downwelling regions (where melt is not produced) and how the release of water via crystallization of silicates interacts with surrounding ambient mantle.

[5] Leahy and Bercovici [2007] address these issues by considering the entrainment of melt at ambient mantle temperatures in the presence of downwelling mantle (Figure 1). In this model, hydrous melt viscously entrained into the transition zone crystallizes as wadsleyite, enriching the melt layer in water. This enriched melt then reacts chemically with overlying solid olivine, melting the downwelling solid mantle. This model is then used to predict the structure of a steady state melt layer above the transition zone; indeed the proposed entrainment mechanism recycles water and silicates very efficiently, and the steady state

¹Department of Geology and Geophysics, Yale University, New Haven, Connecticut, USA.

²Now at Department of Geology and Geophysics, Woods Hole Oceanographic Institution, Woods Hole, Massachusetts, USA.

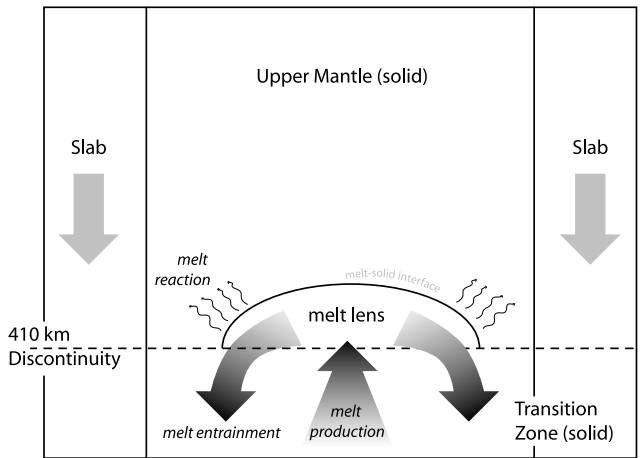


Figure 1. *Leahy and Bercovici* [2007] propose a model for melt layer spreading and entrainment that is driven by convective circulation in the mantle. Hydrated wadsleyite partially melts as it rises above the transition zone and changes phase to olivine. The melt spreads into downwelling regions where it is returned to the transition zone. This process releases water, which reacts with and melts the overlying solid.

length of the melt is well constrained by the water-silicate mass balance.

[6] However, the height of the melt layer predicted by *Leahy and Bercovici* [2007] is only the minimum height required to drive flow in the melt layer. Since the study assumed steady state, it neglects the fact that as the melt spreads toward its steady state length, there is an imbalance between sources and sinks of melt, which would cause the melt layer to increase in volume. Moreover, the model neglects that the melt must spread through more viscous surrounding mantle. As the overlying mantle viscosity is quite large, a significant amount of melt must accumulate before the pressure head is sufficient to force the solid mantle out of the way. *Leahy and Bercovici* [2007] also hypothesize that this mechanism of entrainment and reaction permits the melt layer to spread more rapidly than it would by viscous stresses alone, thus allowing for steady state to be achieved relatively quickly.

[7] Here we develop a framework to examine the fully coupled dynamic system of viscous melt spreading and water-induced melting reactions. The method tracks viscous deformation at the melt-solid interface, while considering the effects of water transport on the stability of the melt phase. This model allows more realistic predictions of melt layer structure (particularly the thickness) in both steady state, as well as for time-dependent behavior. Steady state melt thickness of order 10 km is typical for a wide range of transition zone water contents, mantle viscosities, and melt/solid viscosity ratios. Further, effects of temperature on the wet solidus are found to both enhance melt layer thickness and melt spreading because the phase equilibrium determines the net sources and sinks to the layer. We find that steady state structure can develop on timescales equivalent to supercontinent assembly and breakup, allowing

the mid-ocean ridge system to sample a depleted mantle source.

2. Governing Physics

[8] In this section we describe a method by which a diffusion-limited chemical reaction at an interface is coupled with active viscous deformation. In a general sense, the coupling can be illustrated by a model system where a drop is surrounded by a viscous medium. Given an interface between a drop of melt and the surrounding solid, $\mathcal{R}(x, z, t)$, gravitational settling of the drop induces flow in the solid and therefore advection of reagent in the outer fluid. This perturbs the diffusive equilibrium at the interface, which drives a phase change reaction, creating or consuming melt. This then influences how the drop settles.

[9] In this study we will consider the influence of a water-driven melting reaction on the gravitational collapse of a dense melt. For simplicity, we will neglect the effects of temperature variability on all parameters, including viscosity, water solubility, and diffusion. This assumption is valid in the limit where thermal diffusion is much faster than hydrogen diffusion, and reflects lengthscales over which the system can be considered isothermal. We do, however, investigate how changing ambient mantle temperature affects model results. Further, following *Leahy and Bercovici* [2007], we assume that the melt region is a pure melt lens and not a two phase fluid.

[10] Here we discuss the governing equations for the model, which can be broken into several parts: diffusion of water and the melt-solid reaction (section 2.1), interactions with background flow (section 2.2), and flow induced by the melt-solid boundary (section 2.3). To differentiate between the velocity of the interface and the fluid velocities, we will adopt the notation whereby interface velocities are denoted by $\dot{\mathcal{R}}$ and the fluid velocity of the surrounding media due to motion of the interface by $\tilde{\mathbf{u}}$.

[11] For an interface at position $\mathcal{R}(x, z, t)$ (represented in two dimensions as a parametric curve with time dependent position x, z), we decompose the interface velocity $\dot{\mathcal{R}}$ (equation (1)) into terms representing inflation due to direct sources of melt (supplied by the transition zone) $\dot{\mathcal{R}}^I$, viscous settling $\dot{\mathcal{R}}^V$, and the rate of the melting reaction $\dot{\mathcal{R}}^R$. Our method aims to determine these apparent interfacial velocities and then evolve the interface in time, such that

$$\frac{d\mathcal{R}}{dt} = \dot{\mathcal{R}} = \dot{\mathcal{R}}^I + \dot{\mathcal{R}}^V + \dot{\mathcal{R}}^R \quad (1)$$

[12] In a similar manner, we can decompose the fluid flow field far from the boundary into terms representing the slab-driven far-field flow $\tilde{\mathbf{u}}^S$, net sources of melt $\tilde{\mathbf{u}}^I$, circulation induced by viscous settling of the melt $\tilde{\mathbf{u}}^V$, and circulation induced by volume change due to the melting reaction $\tilde{\mathbf{u}}^R$:

$$\tilde{\mathbf{u}} = \tilde{\mathbf{u}}^S + \tilde{\mathbf{u}}^I + \tilde{\mathbf{u}}^V + \tilde{\mathbf{u}}^R \quad (2)$$

[13] In the subsequent sections, we develop the mathematical framework for this model. In general, the governing equations are valid in three dimensions; however, *Leahy and Bercovici* [2007] suggest two dimensions is sufficient (up to a constant geometric scaling factor) to explore the dynamics

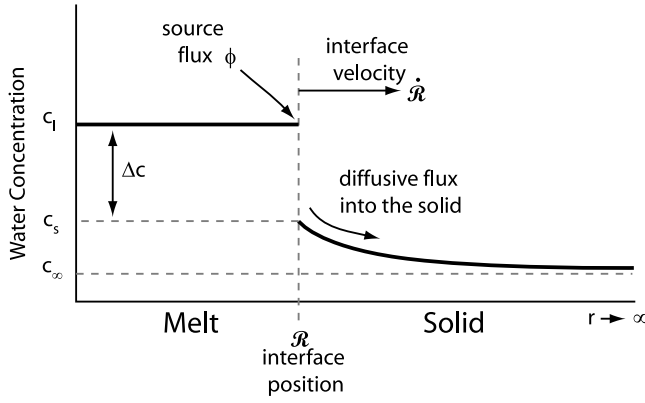


Figure 2. Phase change reaction is mediated by local equilibrium at the melt/solid interface \mathcal{R} . If a source flux ϕ into the boundary is not balanced by diffusion in the solid, melting ensues and the interface proceeds to the right ($\dot{\mathcal{R}} > 0$). If diffusive loss of water exceeds the source flux, crystallization ensues and the interface proceeds to the left ($\dot{\mathcal{R}} < 0$).

of the system, which also has the benefit of simplifying the numerical method.

2.1. Diffusion of Water and the Melt-Solid Reaction

[14] Diffusion-controlled moving interface problems are characterized by diffusion between adjacent media which are coupled via local thermodynamic equilibrium at the interface [e.g., Zener, 1949; Illingworth and Golosnoy, 2005]. In this study, water is the reacting species and its concentration will be labeled c . While water in the exterior solid olivine c_{ol} and water in the melt c_m are generally functions of time and space, several quantities appear in the following equations that are fixed for a given numerical experiment: c_∞ , the background water concentration in the solid upper mantle (typically zero); c_s , the equilibrium water content for solid olivine in contact with a silicate melt; c_ℓ , the equilibrium water content for a melt in contact with solid; c_{wd} , the water content of wadsleyite in the transition zone; and c_{wd}^* , the transition zone water solubility limit. In our system, the concentration of water outside the melt satisfies

$$\frac{\partial c_{ol}}{\partial t} + \tilde{\mathbf{u}}_{ol} \cdot \nabla c_{ol} = \nabla \cdot (\underline{\kappa}_{ol} \cdot \nabla c_{ol}) \quad (3)$$

while the concentration of water inside the melt satisfies

$$\frac{\partial c_m}{\partial t} + \tilde{\mathbf{u}}_m \cdot \nabla c_m = \nabla \cdot (\underline{\kappa}_m \cdot \nabla c_m) \quad (4)$$

[15] In equations (3) and (4), $\tilde{\mathbf{u}}$ is the full mantle flow velocity in its respective medium from equation (2), and $\underline{\kappa}$ is the diffusivity tensor of the reagent. We will assume isotropic diffusivity ($\underline{\kappa} = I\kappa$), and that the solid and melt are in local equilibrium at the contact interface, with water contents c_s and c_ℓ , respectively. By considering the conservation of water through the drop interface, we can relate the

interface velocity due to reaction $\dot{\mathcal{R}}^R = |\dot{\mathcal{R}}^R| \hat{\mathbf{n}}$ to the net flux of water into the interface

$$(c_s - c_\ell) |\dot{\mathcal{R}}^R| = -\kappa_m \nabla c_m \cdot \hat{\mathbf{n}}|_{r=\mathcal{R}^-} + \kappa_{ol} \nabla c_{ol} \cdot \hat{\mathbf{n}}|_{r=\mathcal{R}^+} - c_s \mathbf{u}^R \cdot \hat{\mathbf{n}} + \phi \quad (5)$$

[16] In equation (5), the first and second terms on the right-hand side represent diffusive fluxes in the melt and solid, respectively, evaluated at the interface \mathcal{R} . The third term represents advection of water in the solid in the frame of the interface

$$\mathbf{u}^R = (1 - \frac{\rho_m}{\rho_{ol}}) |\dot{\mathcal{R}}^R| \hat{\mathbf{n}} \quad (6)$$

This term accounts for expansion or compression as melt with density ρ_m changes phase to solid with density ρ_{ol} , and vanishes accordingly when the densities are the same. Because fluid velocities and stresses associated with outside processes (melt spreading or mantle flow) are continuous across the interface, they do not contribute explicitly to the advection term in (5). In our system, the melt is more dense, resulting in flow of solid toward the interface as melting occurs. In the limit that diffusion and advection are negligible, equation (5) reverts to the melting rate given by Leahy and Bercovici [2007, equations (A6)–(A8)].

[17] The term ϕ in equation (5) represents a source flux of reagent. In the absence of a source of water, either via injection of new melt or an external flux, diffusion of water into an infinite solid will eventually lead to the complete crystallization of the melt. In the system considered here ϕ represents the residual water flux released by crystallization of saturated wadsleyite when melt is advected into the wadsleyite stability field (by $\tilde{u}_z^S(x)$, the slab driven flow). From Leahy and Bercovici [2007], the excess water per unit length is defined where the melt layer thickness is nonzero

$$\phi(x) = \begin{cases} 0 & \forall x: \tilde{u}_z^S(x) \geq 0 \\ \tilde{u}_z^S(x) \frac{c_\ell - c_{wd}^*}{1 - c_{wd}^*} & \forall x: \tilde{u}_z^S(x) < 0 \end{cases} \quad (7)$$

[18] While equations (3)–(6) fully characterize the reacting system, we will make a simplifying assumption; we assume that the timescale for diffusion in the solid is much greater than the timescale for mixing in the melt and therefore that $c_m(t, \mathbf{x}) = c_\ell$. This satisfies equation (4) and simplifies equation (5) by forcing the first term on the right to vanish. Figure 2 gives a visual representation of how equation (5) is implemented in our model.

2.2. Interactions With Background Mantle Flow

[19] We assume that the main characteristics of melt production and entrainment are forced by thermally driven convection in the whole mantle. In an internally heated system, flow is primarily slab driven, and upwelling represents a passive return flow. We simplify this assumption

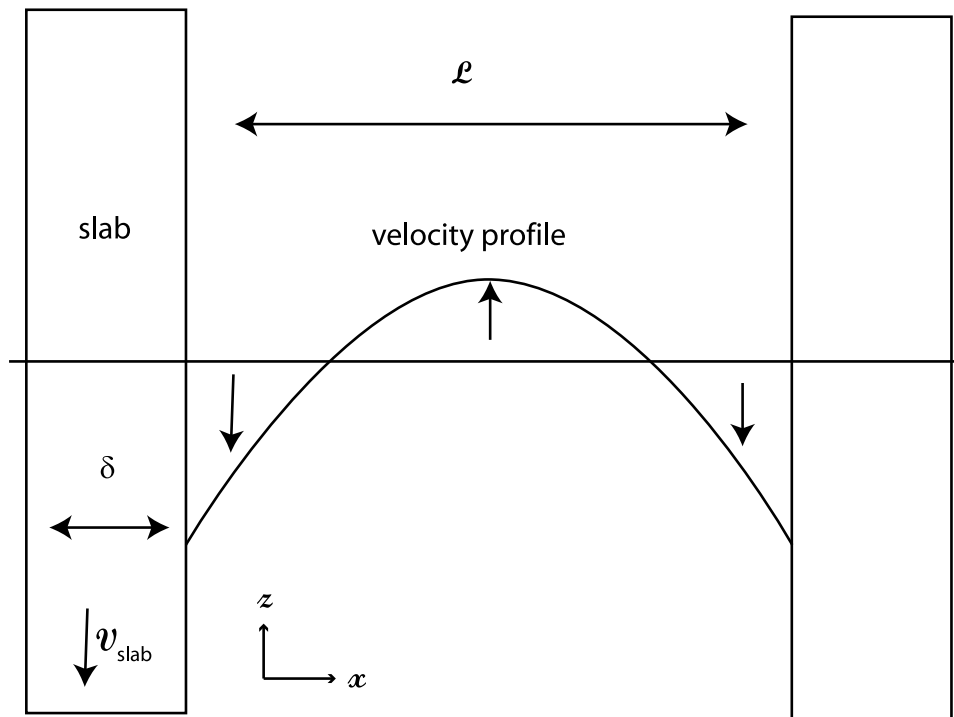


Figure 3. Flow in the model mantle is driven by two parallel descending slabs. The spatial dependence of the velocity field controls the magnitudes and locations of sources and sinks of mass to the melt layer. The following parameters define the flow field: δ , the slab thickness, \mathcal{L} , the distance between slabs, and $\mathcal{V}_{\text{slab}}$, the subduction velocity.

tion by constructing a model system consisting of two slabs descending vertically into the mantle (Figure 3). The bulk-mantle flow field between the slabs $\tilde{\mathbf{u}}^S$ is derived simply as the return flow, following the lubrication assumptions:

$$\tilde{\mathbf{u}}^S(x) = \mathcal{V}_{\text{slab}} \left(6 \left(\frac{\delta}{2\mathcal{L}} + 1 \right) \left(\frac{x}{\mathcal{L}} \right) \left(\frac{x}{\mathcal{L}} - 1 \right) + 1 \right) \hat{\mathbf{z}} \quad (8)$$

where $\mathcal{V}_{\text{slab}}$ is the downwelling slab velocity, δ is the slab thickness, and \mathcal{L} is the distance between the slabs. This mantle flow field determines the locations and magnitudes of sources and sinks of melt and water: melt is produced in mantle upwellings and possibly entrained in mantle downwellings.

2.3. Boundary-Driven Flow

[20] We use a boundary integral formulation to relate the stress and velocity of the melt and solid mantle at the contact interface. This method further permits the calculation of the far-field velocity in either fluid when the interfacial stress and velocity are known. For a review of the treatment of viscous deformation using the boundary integral method, see *Pozrikidis* [2001]. In our system, we assume the 410 km discontinuity is flat, with the melt density intermediate between the density of wadsleyite and olivine. The system is therefore best described as a low viscosity fluid spreading along a fixed boundary plane. Because the spreading is predominantly resisted by the displacement of solid olivine

surrounding the melt, internal viscous drag within the melt has little effect on spreading rate; thus we can assume the basal plane is a free-slip boundary for simplicity in our calculations.

[21] We therefore employ an image formalism (following *Koch and Koch* [1995]), as illustrated in Figure 4, where the boundary plane is the symmetry plane between two identical drops of opposite buoyancy (but similar viscosity) converging toward each other. The position of the melt lens in Figure 4 is given by the solid contour, and its image is given by the dashed contour.

[22] Each point on the boundary $\mathbf{x} = (x, z)$ therefore has a corresponding image point $\mathbf{x}' = (x, -z)$. Stress and interfacial velocity are also reflected through the mirror plane to the image system. All primed variables in what follows represent the image equivalents of the real (unprimed) quantities. This formulation allows the use of the two-dimensional free-space integration kernels for stress and velocity:

$$G_{ji} = -\delta_{ij} \log r + \frac{\hat{x}_i \hat{x}_j}{r^2} \quad \text{and} \quad T_{ijk} = -4 \frac{\hat{x}_i \hat{x}_j \hat{x}_k}{r^4} \quad (9)$$

where $\hat{\mathbf{x}} = \mathbf{x} - \mathbf{x}_0$ and $r = |\hat{\mathbf{x}}|$, with \mathbf{x}_0 an observation point [*Pozrikidis*, 1992]. G_{ji} and T_{ijk} are tensors representing solutions to the Stokes equation for a point stress and point velocity, respectively. We consider contributions to the boundary velocity from gravitational collapse, reactive

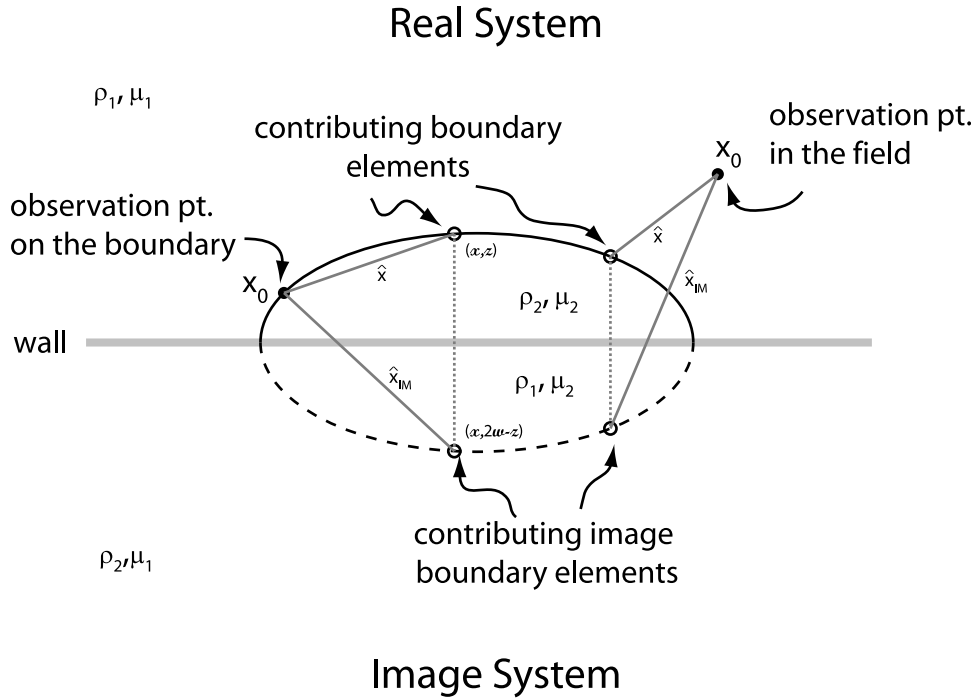


Figure 4. Velocity due to gravitational settling of a drop on a plane wall at an observation point, \mathbf{x}_0 , in the domain, either on or off of the boundary, is determined by considering the contribution of other elements on the boundary in the real and imaginary system. The image system is a physical analogue system of a drop with identical viscosity but opposite buoyancy force rising against a plane wall.

expansion due to the melt-solid density contrast, and melt layer inflation from sources and sinks of melt.

2.3.1. Gravitational Collapse

[23] We relate the velocity of the melt-solid contact interface due to viscous settling $\dot{\mathcal{R}}^V$ at a point \mathbf{x}_0 on the boundary to the hydrostatic stress jump across the interface $\Delta f_i(\mathbf{x}) = \Delta \rho g z \hat{n}_i$ ($\Delta \rho$ represents the density contrast between fluid and melt, and g the gravitational acceleration) following [Pozrikidis, 1992]

$$\begin{aligned} \dot{\mathcal{R}}_j^V(\mathbf{x}_0) = & -\frac{1}{2\pi\mu_{ol}} \frac{1}{1+\lambda} \left(\int_{\mathcal{C}} \mathcal{G}_{ji}(\mathbf{x}, \mathbf{x}_0) \Delta f_i(\mathbf{x}) d\ell(\mathbf{x}) \right. \\ & + \int_{\mathcal{C}_{IM}} \mathcal{G}_{ji}(\mathbf{x}', \mathbf{x}_0) \Delta f'_i(\mathbf{x}') d\ell(\mathbf{x}') \\ & + \frac{1}{2\pi} \frac{1-\lambda}{1+\lambda} \left(\int_{\mathcal{C}} \dot{\mathcal{R}}_i^V(\mathbf{x}) \mathcal{T}_{ijk}(\mathbf{x}, \mathbf{x}_0) \hat{n}_k(\mathbf{x}) d\ell(\mathbf{x}) \right. \\ & \left. + \int_{\mathcal{C}_{IM}} \dot{\mathcal{R}}_i^V(\mathbf{x}') \mathcal{T}_{ijk}(\mathbf{x}', \mathbf{x}_0) \hat{n}'_k(\mathbf{x}') d\ell(\mathbf{x}') \right) \end{aligned} \quad (10)$$

where $\lambda = \frac{\mu_m}{\mu_{ol}}$ is the viscosity ratio between the melt and the overlying solid. Equation (10) is a Fredholm equation of the second kind for $\dot{\mathcal{R}}^V$; by specifying the interfacial stress we can iterate to obtain a solution for the interface settling velocity. The integrals are computed along the contours \mathcal{C} (in the real system) and \mathcal{C}_{IM} (in the image system), and those denoted \mathcal{PV} are to be performed in the principal value sense [Pozrikidis, 2002, pp. 69–70]. When both the stress and velocity at the interface are known, we can calculate the contribution

of viscous settling to the fluid velocity $\tilde{\mathbf{u}}^V$ in the far field using the following equation:

$$\begin{aligned} \tilde{u}_j^V(\mathbf{x}_0) = & -\frac{1}{4\pi\mu_{ol}} \left(\int_{\mathcal{C}} \mathcal{G}_{ji}(\mathbf{x}, \mathbf{x}_0) \Delta f_i(\mathbf{x}) d\ell(\mathbf{x}) \right. \\ & + \int_{\mathcal{C}_{IM}} \mathcal{G}_{ji}(\mathbf{x}', \mathbf{x}_0) \Delta f'_i(\mathbf{x}') d\ell(\mathbf{x}') \\ & + \frac{1-\lambda}{4\pi} \left(\int_{\mathcal{C}} \dot{\mathcal{R}}_i^V(\mathbf{x}) \mathcal{T}_{ijk}(\mathbf{x}, \mathbf{x}_0) \hat{n}_k(\mathbf{x}) d\ell(\mathbf{x}) \right. \\ & \left. + \int_{\mathcal{C}_{IM}} \dot{\mathcal{R}}_i^V(\mathbf{x}') \mathcal{T}_{ijk}(\mathbf{x}', \mathbf{x}_0) \hat{n}'_k(\mathbf{x}') d\ell(\mathbf{x}') \right) \end{aligned} \quad (11)$$

2.3.2. Reactive Expansion

[24] As described in section 2.1, a difference in density between the melt and solid excites flow due to expansion (or contraction) in the far field. The interfacial velocity \mathbf{u}^R is given by equation (6) and can be related to interfacial stress f_i^R through

$$\begin{aligned} u_j^R(\mathbf{x}_0) = & -\frac{1}{2\pi\mu_{ol}} \left(\int_{\mathcal{C}} \mathcal{G}_{ji}(\mathbf{x}, \mathbf{x}_0) f_i^R(\mathbf{x}) d\ell(\mathbf{x}) \right. \\ & + \int_{\mathcal{C}_{IM}} \mathcal{G}_{ji}(\mathbf{x}', \mathbf{x}_0) f_i^{RIM}(\mathbf{x}') d\ell(\mathbf{x}') \\ & + \frac{1}{2\pi} \left(\int_{\mathcal{C}} u_i^R(\mathbf{x}) \mathcal{T}_{ijk}(\mathbf{x}, \mathbf{x}_0) \hat{n}_k(\mathbf{x}) d\ell(\mathbf{x}) \right. \\ & \left. + \int_{\mathcal{C}_{IM}} u_i^R(\mathbf{x}') \mathcal{T}_{ijk}(\mathbf{x}', \mathbf{x}_0) \hat{n}'_k(\mathbf{x}') d\ell(\mathbf{x}') \right) \end{aligned} \quad (12)$$

Table 1. Physical and Material Parameters Used During the Calculations^a

Symbol	Property	Value/Range
Fixed		
$\mathcal{V}_{\text{slab}}$	slab velocity	10^{-10} m/s
\mathcal{L}	distance between slabs	1000 km
δ	slab thickness	100 km
ρ_m	melt density	3400 kg/m ³
ρ_{ol}	solid density	3300 kg/m ³
c_{wd}^*	wadsleyite water saturation	3 wt%
g	gravitational acceleration	9.81 m/s ²
κ_{ol}	hydrogen diffusivity in olivine	10^{-8} m ² /s
Varied		
c_{wd}	initial transition zone water content	0.1–3 wt%
λ	melt/solid viscosity ratio	$1-10^{-5}$
c_{ℓ}	olivine liquidus water content	15–2.5 wt%
c_s	olivine solidus water content	0.06–0.01 wt%
μ_{ol}	viscosity of solid mantle	$10^{20}-10^{23}$ Pa s

^aThe first set represent parameters fixed for the purposes of this study, while the second set are systematically varied.

[25] We can then use the stress and velocity at the interface to calculate the velocity due to the phase change $\tilde{\mathbf{u}}^R$ in the far field:

$$\begin{aligned} \tilde{u}_j^R(\mathbf{x}_0) = & -\frac{1}{4\pi\mu_{\text{ol}}} \left(\int_C \mathcal{G}_{ji}(\mathbf{x}, \mathbf{x}_0) f_i^R(\mathbf{x}) d\ell(\mathbf{x}) \right. \\ & + \int_{C_{\text{IM}}} \mathcal{G}_{ji}(\mathbf{x}', \mathbf{x}_0) f_i^{R'}(\mathbf{x}') d\ell(\mathbf{x}') \\ & + \frac{1}{4\pi} \left(\int_C u_i^R(\mathbf{x}) \mathcal{T}_{ijk}(\mathbf{x}, \mathbf{x}_0) \hat{n}_k(\mathbf{x}) d\ell(\mathbf{x}) \right. \\ & \left. \left. + \int_{C_{\text{IM}}} u_i^{R'}(\mathbf{x}') \mathcal{T}_{ijk}(\mathbf{x}', \mathbf{x}_0) \hat{n}'_k(\mathbf{x}') d\ell(\mathbf{x}') \right) \right) \end{aligned} \quad (13)$$

2.3.3. Melt Layer Inflation

[26] In the model proposed by *Leahy and Bercovici* [2007], flow in the mantle caused by slab subduction determines the locations of sources of melt (in upwelling regions) and sinks of melt (in downwelling regions). Because we assume the melt is incompressible, the net source per unit length, \mathcal{S} , contributes directly to the vertical velocity of the interface due to inflation or deflation:

$$\mathcal{S}(x) = \hat{\mathcal{R}}^I = \begin{cases} \tilde{u}_z^S(x) \frac{c_{\ell} - c_{\text{wd}}}{c_{\ell} - c_s} \hat{\mathbf{z}} & \forall x: \tilde{u}_z^S(x) \geq 0 \\ \tilde{u}_z^S(x) \frac{1 - c_{\ell}}{1 - c_{\text{wd}}^*} \hat{\mathbf{z}} & \forall x: \tilde{u}_z^S(x) < 0 \end{cases} \quad (14)$$

where $u_z^S(x)$ is the vertical component of mantle flow from equation (8). In upwelling areas, the source is the melt produced by equilibrium (batch) melting of upwelling mantle with a given water content (for further discussion, see *Leahy and Bercovici* [2007]).

[27] Having calculated the instantaneous velocity of the boundary due to sources and sinks of mass, we can solve for the instantaneous stress on the boundary due to expansion f_i^I

using the following boundary integral equation [after *Pozrikidis*, 2002]:

$$\begin{aligned} \hat{\mathcal{R}}_j^I(\mathbf{x}_0) = & -\frac{1}{2\pi\mu_{\text{ol}}} \left(\int_C \mathcal{G}_{ji}(\mathbf{x}, \mathbf{x}_0) f_i^E(\mathbf{x}) d\ell(\mathbf{x}) \right. \\ & + \int_{C_{\text{IM}}} \mathcal{G}_{ji}(\mathbf{x}', \mathbf{x}_0) f_i^I(\mathbf{x}') d\ell(\mathbf{x}') \\ & + \frac{1}{2\pi} \left(\int_C \hat{\mathcal{R}}_i^I(\mathbf{x}) \mathcal{T}_{ijk}(\mathbf{x}, \mathbf{x}_0) \hat{n}_k(\mathbf{x}) d\ell(\mathbf{x}) \right. \\ & \left. \left. + \int_{C_{\text{IM}}} \hat{\mathcal{R}}_i^I(\mathbf{x}') \mathcal{T}_{ijk}(\mathbf{x}', \mathbf{x}_0) \hat{n}'_k(\mathbf{x}') d\ell(\mathbf{x}') \right) \right) \end{aligned} \quad (15)$$

[28] We can then use the stress and velocity at the interface (which satisfy equation (15)) to calculate the fluid velocity due to expansion $\tilde{\mathbf{u}}^I$ in the far field:

$$\begin{aligned} \tilde{u}_j^I(\mathbf{x}_0) = & -\frac{1}{4\pi\mu_{\text{ol}}} \left(\int_C \mathcal{G}_{ji}(\mathbf{x}, \mathbf{x}_0) f_i^I(\mathbf{x}) d\ell(\mathbf{x}) \right. \\ & + \int_{C_{\text{IM}}} \mathcal{G}_{ji}(\mathbf{x}', \mathbf{x}_0) f_i^I(\mathbf{x}') d\ell(\mathbf{x}') \\ & + \frac{1}{4\pi} \left(\int_C \hat{\mathcal{R}}_i^I(\mathbf{x}) \mathcal{T}_{ijk}(\mathbf{x}, \mathbf{x}_0) \hat{n}_k(\mathbf{x}) d\ell(\mathbf{x}) \right. \\ & \left. \left. + \int_{C_{\text{IM}}} \hat{\mathcal{R}}_i^I(\mathbf{x}') \mathcal{T}_{ijk}(\mathbf{x}', \mathbf{x}_0) \hat{n}'_k(\mathbf{x}') d\ell(\mathbf{x}') \right) \right) \end{aligned} \quad (16)$$

2.4. Nondimensionalization

[29] Our system involves two competing timescales, $\tau_D = \frac{a^2}{\kappa_{\text{ol}}}$ for diffusion of water over a length scale a and $\tau_S = \frac{\mu_{\text{ol}}}{\Delta\rho g a}$ for gravitational collapse of a drop of radius a . The length scale a is chosen such that

$$\frac{\tau_D}{\tau_S} = \frac{\Delta\rho g a^3}{\kappa_{\text{ol}}\mu_{\text{ol}}} = 1 \quad (17)$$

We nondimensionalize time by τ_D , length by a , concentration by $\Delta c = c_{\ell} - c_s$, and stress by $\Delta\rho g a$. However, computational results in Table 1 are rescaled based on approximate values of appropriate material properties resulting in dimensional predictions.

3. Numerical Method

[30] To characterize the reactive spreading of the melt layer in two dimensions, we track the location of the melt-solid interface. In the numerical scheme, the interface is discretized as a one-dimensional mesh. To compute the interface velocity, we track the transport of water in the solid mantle. This is accomplished by superimposing a two-dimensional cartesian grid on the interface mesh, where the grid resolves water content in both the interior and exterior fluids. When referring to mesh points or mesh elements, we are referring to points on the melt-solid interface; when referring to grid points we are referring to interior points in the solid and the melt.

[31] Solving the full, coupled problem can be broken into six steps: (1) diffusive flux of water through the interface (section 3.1); (2) interface velocity with known interfacial

stress, where we solve for motion of the interface due to gravitational forcing (section 3.2); (3) interface stress with known interfacial velocity, where we solve for the interfacial stress due to reactive and inflationary boundary motion (section 3.3); (4) computation of field velocity, where we compute and combine all elements of the velocity in media on either side of the interface (section 3.4); (5) multigrid method for water transport equation, where we use the field velocity to update water concentration in the solid domain for the next iteration (section 3.5); (6) evolution of the interface mesh, where we update the position of the mesh for the next iteration (section 3.6).

[32] The initial conditions are as follows: an initial position of the mesh is chosen, spanning the upwelling region at the center of the domain with a finite height equivalent to three grid points. This permits melt to accumulate in the upwelling region. The mesh is an open curve of e mesh elements, which are approximated as straight lines joining $e + 1$ mesh points. The end points of the mesh are fixed to the mirror plane but are permitted to move horizontally along this boundary. The cartesian grid is of size $(2^n + 1) \times (2^n + 1)$. The water content in the melt (on grid points inside the mesh) is held constant and is masked in all computations. Water content in the solid mantle (on grid points outside the mesh) is initially set to a dry, background value c_∞ .

3.1. Diffusive Flux of Water Through the Interface

[33] Equation (5) requires an estimate of the diffusive flux of water in the solid away from the boundary in order to calculate the velocity of the interface due to the melting reaction. This estimate must be calculated at each of the $e + 1$ mesh points individually. For each mesh point \mathbf{x}_0 , we first linearly interpolate the water concentration field at two points normal to the melt-solid interface, $c_1 = c(\mathbf{x}_1)$ and $c_2 = c(\mathbf{x}_2)$. These points are located at $\mathbf{x}_1 = \mathbf{x}_0 + r_\phi \hat{\mathbf{n}}$ and $\mathbf{x}_2 = \mathbf{x}_0 + 2r_\phi \hat{\mathbf{n}}$, where r_ϕ is chosen to be sufficiently large such that the concentration field is smooth (see section 3.5). These two points and the concentration at the boundary $c_0 = c_\ell / \Delta c$ are fit by a parabola:

$$c(r) = c_0 + \left(\frac{2c_1}{r_\phi} - \frac{3c_0}{2r_\phi} - \frac{c_2}{2r_\phi} \right) r + \left(\frac{c_0}{2r_\phi^2} + \frac{c_2}{2r_\phi^2} - \frac{c_1}{r_\phi^2} \right) r^2 \quad (18)$$

The flux at the interface is then calculated as the derivative of the parabola evaluated at $\mathbf{x}_0 + .5r_\phi \hat{\mathbf{n}}$:

$$\left. \frac{\partial c}{\partial r} \right|_{r=.5r_\phi} = \left(\frac{2c_1}{r_\phi} - \frac{3c_0}{2r_\phi} - \frac{c_2}{2r_\phi} \right) + \left(\frac{c_0}{r_\phi^2} + \frac{c_2}{r_\phi^2} - \frac{2c_1}{r_\phi^2} \right) r \Big|_{r=.5r_\phi} \quad (19)$$

3.2. Boundary Velocity With Known Interfacial Stress

[34] Given the hydrostatic stress jump across the interface, we calculate the fluid velocity at the interface. For simplicity, we assume that the velocity and stress are constant along each element e of the mesh, and we recast the boundary integral equation (10) as a linear system (after

appropriate nondimensionalization), following *Pozrikidis* [2002, pp. 63–75]:

$$\begin{aligned} \dot{\mathcal{R}}_j(\mathbf{x}_0) = & \sum_e \alpha z |^e \hat{n}_i^e A_{ij}^e(\mathbf{x}_0) + \sum_e e \beta \dot{\mathcal{R}}_i^e B_{ij}^e(\mathbf{x}_0) \\ & - \sum_{e'} \alpha z |^{e'} \hat{n}_i^{e'} A_{ij}^{e'}(\mathbf{x}_0) + \sum_{e'} \beta \dot{\mathcal{R}}_i^{e'} B_{ij}^{e'}(\mathbf{x}_0) \end{aligned} \quad (20)$$

[35] The point \mathbf{x}_0 is an observation point located on the mesh, and primes refer to the image system as before (e' is an image element). The negative sign leading the third term is a result of the mapping of hydrostatic stress to the image system. For each element e , the second rank influence tensors \mathbf{A}^e and \mathbf{B}^e are given by

$$A_{ij}^e(\mathbf{x}_0) = - \int_e \mathcal{G}_{ji}(\mathbf{x}_0, \mathbf{x}) d\ell \quad (21)$$

and

$$B_{ij}^e(\mathbf{x}_0) = \int_C^{\mathcal{P}\mathcal{V}} \mathcal{T}_{ijk}(\mathbf{x})(\mathbf{x}_0, \mathbf{x}) \hat{n}_k^e(\mathbf{x}) d\ell \quad (22)$$

where e' is substituted for e in integrals over image elements. The constants α and β are

$$\alpha = \frac{1}{2\pi} \frac{1}{1 + \lambda} \quad (23)$$

$$\beta = \frac{1}{2\pi} \frac{1 - \lambda}{1 + \lambda} \quad (24)$$

[36] For nonsingular elements, the integrals are performed using a six-point Gaussian quadrature scheme [*Press et al.*, 1992, pp. 145–146]. For singular elements, where \mathbf{x} approaches the observation point \mathbf{x}_0 , the integrals are calculated analytically [*Pozrikidis*, 2002, p. 70]. We then iterate over $\dot{\mathcal{R}}$ until convergence to solve for the boundary velocity on each element.

3.3. Boundary Stress With Known Interfacial Velocity

[37] When the boundary velocity is specified, such as in equations (12) and (15), we must calculate the resulting interfacial stress in order to compute the far-field mantle velocity. Each of these equations, when nondimensionalized, may be recast as a linear system as in section 3.2:

$$\begin{aligned} \dot{\mathcal{R}}_j(\mathbf{x}_0) = & \sum_e \gamma f_i^e A_{ij}^e(\mathbf{x}_0) + \sum_e \gamma \dot{\mathcal{R}}_i^e B_{ij}^e(\mathbf{x}_0) \\ & + \sum_{e'} \gamma f_i^{e'} A_{ij}^{e'}(\mathbf{x}_0) + \sum_{e'} \gamma \dot{\mathcal{R}}_i^{e'} B_{ij}^{e'}(\mathbf{x}_0) \end{aligned} \quad (25)$$

where again \mathbf{x}_0 is a point on the mesh, primed elements are in the image system, and the influence matrices are given by equations (21) and (22), and $\gamma = 1/2\pi$. This linear system can be directly inverted for the interfacial stress f_i^e on each element, which is used as a jump condition for far field flow. Here the inversion is accomplished via LU decomposition [*Press et al.*, 1992, pp. 38–39].

3.4. Computation of Field Velocity

[38] Having obtained values for stress and velocity on each element, we can then calculate the velocity at an observation point \mathbf{x}_0 in the outer medium using equations (11), (13), and (16). These equations discretize as

$$\begin{aligned} \tilde{u}_j^V(\mathbf{x}_0) = & \sum_e \alpha z |^e \hat{n}_i^e A_{ij}^e(\mathbf{x}_0) + \sum_e \beta (\dot{\mathcal{R}}^V)_i^e B_{ij}^e(\mathbf{x}_0) \\ & + \sum_e \alpha z |^{e'} \hat{n}_i^{e'} A_{ij}^{e'}(\mathbf{x}_0) + \sum_e \beta (\dot{\mathcal{R}}^V)_i^{e'} B_{ij}^{e'}(\mathbf{x}_0) \end{aligned} \quad (26)$$

$$\begin{aligned} \tilde{u}_j^R(\mathbf{x}_0) = & \sum_e \gamma (f^R)_i^e A_{ij}^e(\mathbf{x}_0) + \sum_e \gamma (\dot{\mathcal{R}}^R)_i^e B_{ij}^e(\mathbf{x}_0) \\ & + \sum_e \gamma (f^R)_i^{e'} A_{ij}^{e'}(\mathbf{x}_0) + \sum_e \gamma (\dot{\mathcal{R}}^R)_i^{e'} B_{ij}^{e'}(\mathbf{x}_0) \end{aligned} \quad (27)$$

and

$$\begin{aligned} \tilde{u}_j^I(\mathbf{x}_0) = & \sum_e \gamma (f^I)_i^e A_{ij}^e(\mathbf{x}_0) + \sum_e \gamma (\dot{\mathcal{R}}^I)_i^e B_{ij}^e(\mathbf{x}_0) \\ & + \sum_e \gamma (f^I)_i^{e'} A_{ij}^{e'}(\mathbf{x}_0) + \sum_e \gamma (\dot{\mathcal{R}}^I)_i^{e'} B_{ij}^{e'}(\mathbf{x}_0) \end{aligned} \quad (28)$$

respectively. The influence matrices are nonsingular in equations (26)–(28) and can therefore be evaluated directly and the results substituted into equation (2). In this manner, we calculate the full field velocity at each point on the cartesian grid, which is then used in the solution of the water transport equation.

3.5. Multigrid Method for Water Transport Equation

[39] The water concentration field, the solution to equation (3), is solved over a square domain spanning the distance between slabs in the model mantle. We use a standard multigrid method (after *Press et al.* [1992, chap. 19]), with a Crank-Nicholson method to difference the operators in time, and centered finite-difference operators for the spatial derivatives [*Press et al.*, 1992]. The advection terms were treated using the Adams-Bashforth method. The multigrid solver was benchmarked against several simple analytic solutions to time-dependent diffusion problems (for example, the decay rate of a sinusoidal perturbation), with varying boundary conditions and imposed velocity fields [*Leahy*, 2008].

[40] In order to solve the diffusion equation in the neighborhood of the spreading melt lens, we make several simplifying assumptions. First, while the flows calculated via the boundary integral method are defined over all space, we will solve the diffusion equation over a finite domain on a cartesian grid. This domain is chosen such that it extends far from the lens, and we take care to check whether edges of the domain influence the evolution of the melt over the course of a simulation. Second, we choose the edge boundary conditions to be insulating to water diffusion, therefore ensuring flux out of the domain of interest is purely advective, which helps decrease the influence of the edges on the melting reaction rate.

[41] Third, we use the mesh to define a mask on the grid in the shape of the drop. Grid points inside the drop shape are set to the surface solid concentration c_s during each

iteration. This allows us to treat the diffusion from an arbitrary shape but requires our grid spacing to be fine enough to resolve small-scale features of the mesh. This technique is similar to limiting curvature in the mesh as described in other studies [*Pozrikidis*, 2002]. Regardless of the grid spacing, the concentration field is rough within two grid spaces of the boundary due to the roughness of the mask. This necessitates precautions when calculating the diffusive flux away from the mesh, particularly in the choice of r_ϕ as in section 3.1. The ability of our benchmarks (section 3.7) to reproduce analytic solutions for interface growth and diffusive flux suggests that accuracy is not sacrificed through these approximations.

3.6. Evolution of the Mesh

[42] The final step in the calculation is to evolve the position of the mesh in time. We simply use the Euler Method to integrate equation (1) and thereby calculate the position of the mesh at the next iteration $i + 1$:

$$\mathbf{x}^{i+1} = \mathbf{x}^i + (\dot{\mathcal{R}}^I + \dot{\mathcal{R}}^V + \dot{\mathcal{R}}^R) \Delta t^i \quad (29)$$

The time interval Δt^i is dynamically determined at each iteration and is calculated to ensure compliance with the Courant-Friedrichs-Lewy conditions [*Press et al.*, 1992, p. 829], using the minimum of a diffusive time step, an advective time step, and a time step derived from interface mobility (the mesh should not move rapidly through the grid). The updated melt-solid boundary and water concentration field are then used to begin the next iteration.

3.7. Computations

[43] The numerical method was benchmarked against several analytic solutions with partial coupling to ensure the accuracy of the full coupled solutions, an example of which is the diffusive crystallization of a water-rich drop (with no gravitational collapse). Full details of the benchmarks are presented by *Leahy* [2008].

[44] Model parameters are listed in Table 1. For the purposes of this study, we leave many of the parameters fixed at plausible values, including those representing the density contrast and the size of the domain. We vary less well known parameters such as viscosity ratio, initial transition zone water content, bulk mantle viscosity, and local equilibrium condition in order to determine relationships between these parameters and melt layer structure.

4. Results

[45] In this section we will investigate how our model responds to changes in physical parameters. We will focus in particular on how melt layer extent and thickness vary with time. These two quantities are the best candidates for seismic investigation in the mantle.

4.1. Melt Spreading Rates

[46] We first consider how viscous settling, interface reaction, and source/sink flow control melt spreading rate (Figure 5). This provides a simple illustration of how our model captures the essential physics of the problem and further allows for a benchmark between our results and previous efforts; we find our results for constant-volume

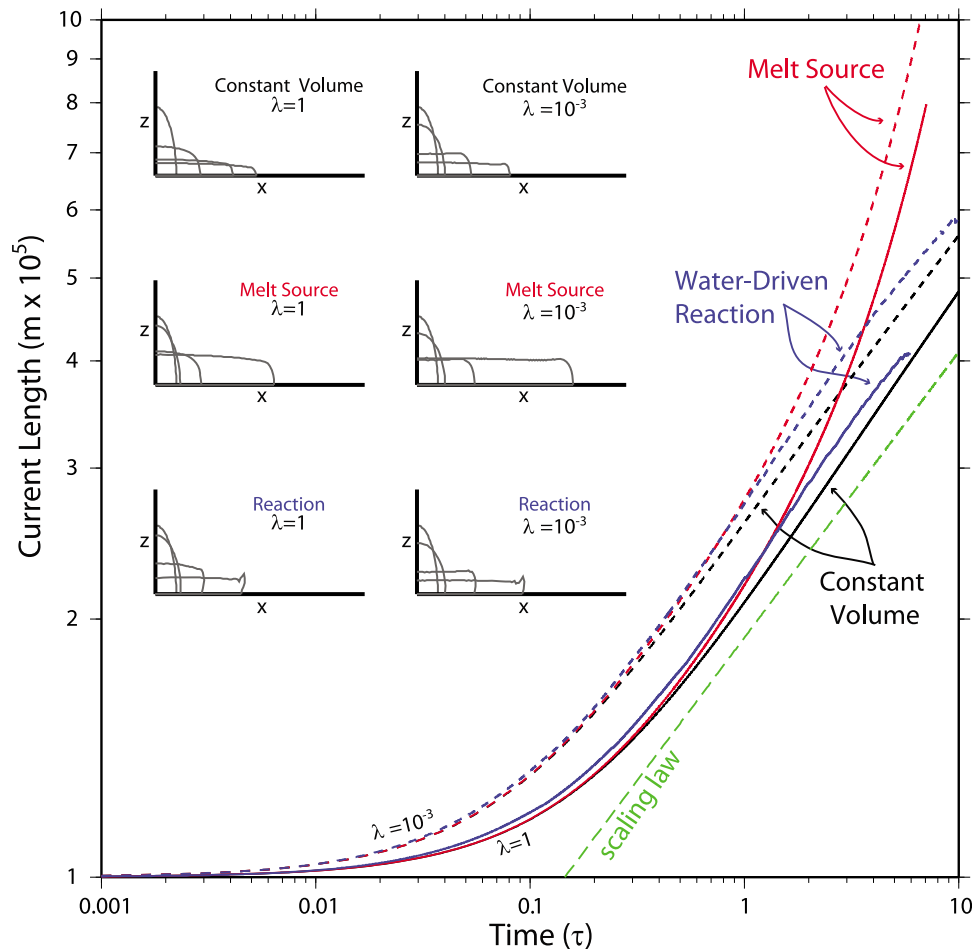


Figure 5. Plotted are the length of gravity currents versus time for three end-member cases with no mass sink; spreading due to excess water release (blue lines), constant volume gravitational collapse (black lines), and melt source-driven flow (red lines). Solid and dashed lines refer to a viscosity ratio between the fluids of $\lambda = 1$ and $\lambda = 10^{-3}$, respectively. These results are compared to a scaling law (green-dashed line) balancing viscous drag with gravitational forces [Lister and Kerr, 1989]. Inset in the frame are actual interface solutions at $\tau = 0, 0.1, 1, 5$.

lens spreading compare favorably with previous calculations [Koch and Koch, 1995] and a simple scaling analysis where gravitational forces are balanced by viscous drag (green dashed line, after Lister and Kerr [1989]). The magnitudes of sources of melt and water used in this calculation are of the same order as might be expected in the mantle, and are obtained from the slab-driven flow field. We find that the reaction-driven flow resembles source-driven flow and is significantly faster than gravitational (buoyancy-driven) collapse alone. Because we neglect a sink of mass in order to focus on the spreading rate, steady state solutions are not possible. These results indicate that the primary impact of the melting reaction on spreading rate is through the addition of melt to the lens.

[47] The inset in Figure 5 displays the actual melt shapes for $\tau = 0, 0.1, 1, 5$ for different viscosity ratios and end-member cases. The constant volume solutions are characterized by almost self-similar collapse as is expected. Source-fed currents are thicker and extend further. In all cases, decreasing the viscosity ratio leads to a more vertical current nose and more rectangular overall shape.

4.2. Diffusion in the Solid

[48] Given sources and sinks of melt due to upwelling and downwelling at the 410 km discontinuity, we examine the influence of diffusive loss of water into the solid mantle and the melting reaction at the lens interface on melt spreading. As a control case, we determine the time-dependent structure of a melt layer driven only by source/sink flow, with no excess water (which would otherwise react with and diffuse into the surrounding solid).

[49] Considered on its own, diffusive loss of water to the solid results in crystallization and is effectively a sink of mass from the current. However, because the solid has lower water storage capacity than the melt, and diffusion is slow, this sink is small compared to the influx and efflux of melt from upwelling and downwelling mantle flow. The effect of diffusion into the solid is to shorten the steady-state length of the current but at a level that is indistinguishable from the control case.

[50] In Figure 6, we show the final shape, water concentration field, and velocity field of a simulation run with full

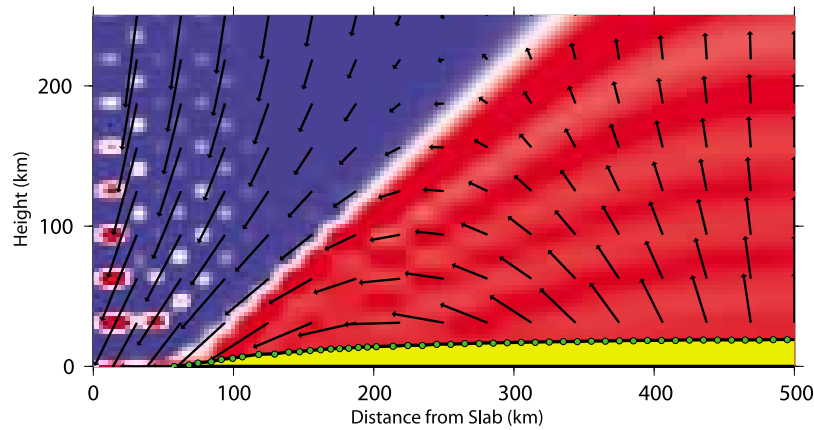


Figure 6. Plotted are the final shape of the melt layer (green circles, yellow indicates melt), the water concentration field (background color, blue is water poor and red is water rich), and the external velocity field (black arrows). The magnitude of diffusion is small relative to source-sink driven flow, and it is ignored for subsequent calculations.

diffusive coupling. Because the effects of diffusion are small, we ignore diffusive loss of water to the solid mantle (i.e., the second term on the right of equation (5) is assumed to be zero) in further calculations. This assumption ignores the feedback between spreading-induced advection in the mantle and diffusive loss of water from the melt layer; this effect is more significant at smaller length scales where diffusive fluxes are larger. We therefore predict that the water distribution in the upper mantle is elevated relative to unfiltered mantle and that sharp gradients in water content will be expected in the vicinity of changes in mantle flow patterns.

4.3. Effect of Melt-Solid Viscosity Ratio

[51] Following the tests illustrated in section 4.2, we next determine the influence of major parameters such as initial transition zone water content c_{wd} , viscosity ratio λ , mantle viscosity μ_{ol} , and temperature on melt spreading and structure. Simulation parameters considered in this and subsequent sections are given in Table 2.

[52] The viscosity ratio λ governs the mechanical coupling between the solid and melt. For a given transition zone water content $c_{wd} = 0.3$ wt% and mantle viscosity $\mu_{ol} = 10^{21}$ Pa s, we vary λ between 10^{-5} and 10^0 (cases 1–6). Figures 7a and 7b show the time evolution of the melt layer thickness and extent, respectively. Low-amplitude (relative to current thickness and extent) noise begins when the melt layer reaches the downwelling regions (approximately 640 km) but is an artifact of the numerical method and indicates difficulty resolving the nose of the current. We consider the nose of the current to be the last point on the interface mesh, but as entrainment proceeds additional points on the mesh are entrained to the interface. We remove extraneous points (with zero height), and this results in oscillations of the models' current length. The data have been smoothed using a moving-window Gaussian filter, resulting in an increase in clarity especially at long times.

[53] Figure 7c shows the time-independent melt layer thickness (diamonds, left axis) and time to steady structure (circles, right axis) versus λ . Owing to high-frequency oscillations, steady structure is inferred if the fractional

Table 2. Parameters for Computational Simulations Described in Section 4^a

Run	\mathcal{V}_{slab}	δ	\mathcal{L}	ρ_{ol}	ρ_m	μ_{ol}	λ	κ_{ol}	c_ℓ	c_s	c_{wd}^*	c_{wd}	Notes
1	10^{-10}	10^5	10^6	3300	3400	10^{21}	10^{-3}	10^{-8}	15	0.06	3	.3	default, 1600 K
2							10^0						sensitivity to viscosity ratio
3							10^{-1}						
4							10^{-2}						
5							10^{-4}						
6							10^{-5}						
7												0.1	sensitivity to TZ water content
8												0.2	
9												0.4	
10												0.5	
11												0.6	
12						10^{20}	10^{-3}						sensitivity to exterior viscosity
13						10^{22}	10^{-3}						
14						10^{23}	10^{-3}						
15									12.5	0.05			T = 1700 K
16									10.0	0.04			T = 1800 K
17									7.5	0.03			T = 1900 K

^aSymbol definitions and units are given in Table 1, and blank column entries reflect usage of default values.

Table 3. Trends Observed in Steady State From Simulations Described in Table 2

	Melt Layer Extent	Melt Layer Thickness	Timescale
Melt viscosity increases	constant	increases	increases
TZ water content increases	increases	increases	decreases
Solid viscosity increases	constant	increases	increases
Temperature increases	constant	increases	decreases

change in the average current length over one numerical time step is less than 10^{-3} . A steady length indicates that there is no net source of mass to the melt layer.

[54] Both steady height and length, and the time necessary to achieve steady structure, vary significantly with increasing viscosity ratio, especially at large λ . However, for small λ (less than 10^{-2}) there is almost no variation in either

maximum melt layer height or time to steady structure (Figure 7c); this is because the coefficients in front of the single and double layer potentials (equation (10)) saturate. In the small λ limit, spreading is controlled by viscous drag in the outer fluid, and is not sensitive to the melt viscosity. Examples of time-dependent solutions for the gravity current shape are shown in Figure 8 for two different values of λ .

4.4. Effect of Transition Zone Water Content

[55] Transition zone water content, c_{wd} , determines the magnitude of the influx of melt to the melt lens by changing the melt fraction. Calculations in this section are performed with parameters $\lambda = 10^{-3}$ and $\mu_{ol} = 10^{21}$ Pa s at 1600 K (cases 1, 7–11). In Figure 9, we show how the melt layer structure depends on water content. The primary response to an increase in water content (and therefore in the melt

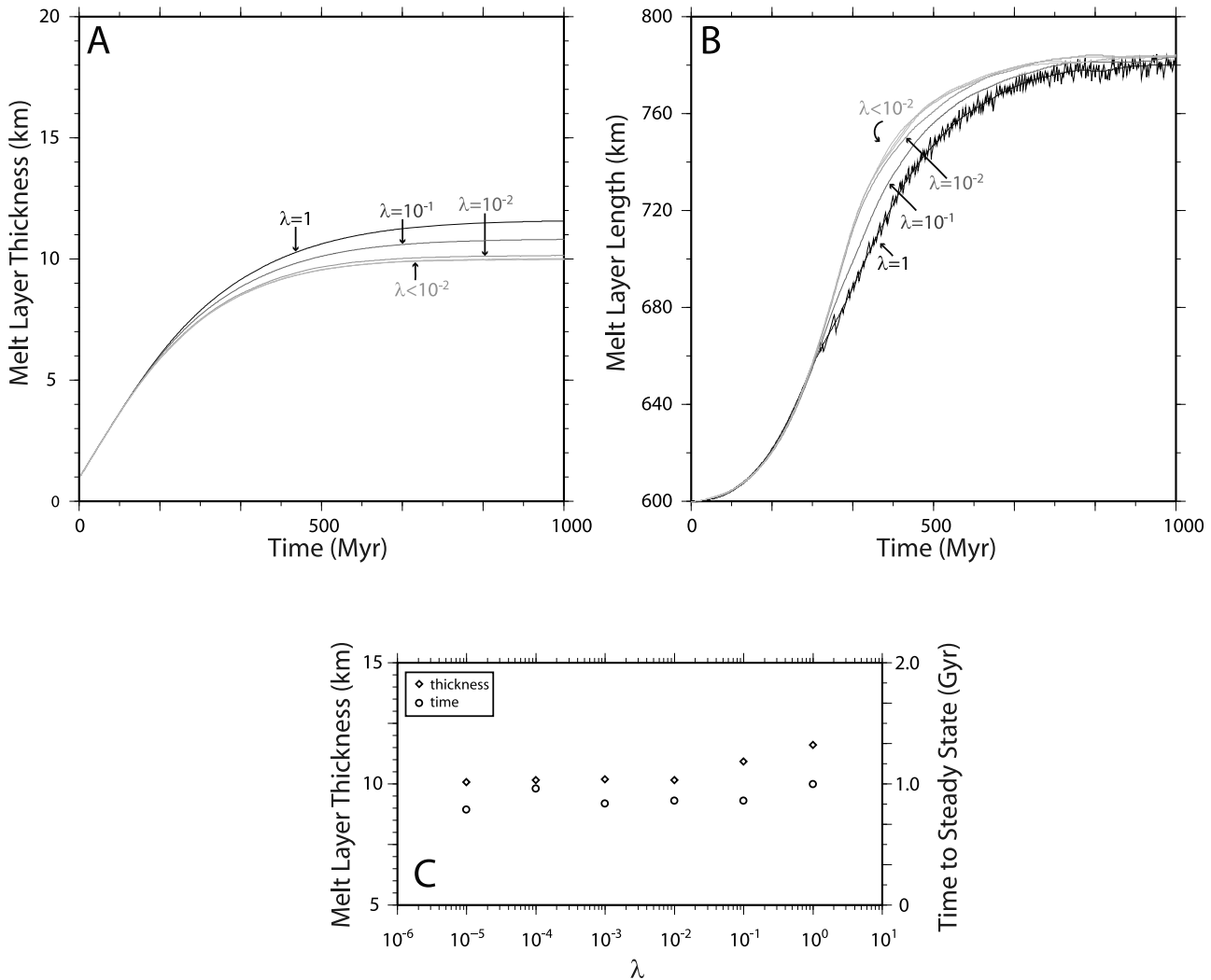


Figure 7. (a) Thickness of the melt layer versus time for an increasing viscosity ratio between the melt and the solid. Lighter tones indicate stronger contrasts. (b) Length of the melt layer versus time for increasing viscosity ratio (same color scale as in Figure 7a). Gaussian smoothing has been applied in all cases, but unsmoothed data is also plotted for $\lambda = 1$ to demonstrate range of uncertainty. (c) Steady state melt layer thickness (left axis, diamonds) and time to steady structure (right axis, circles) versus viscosity ratio.

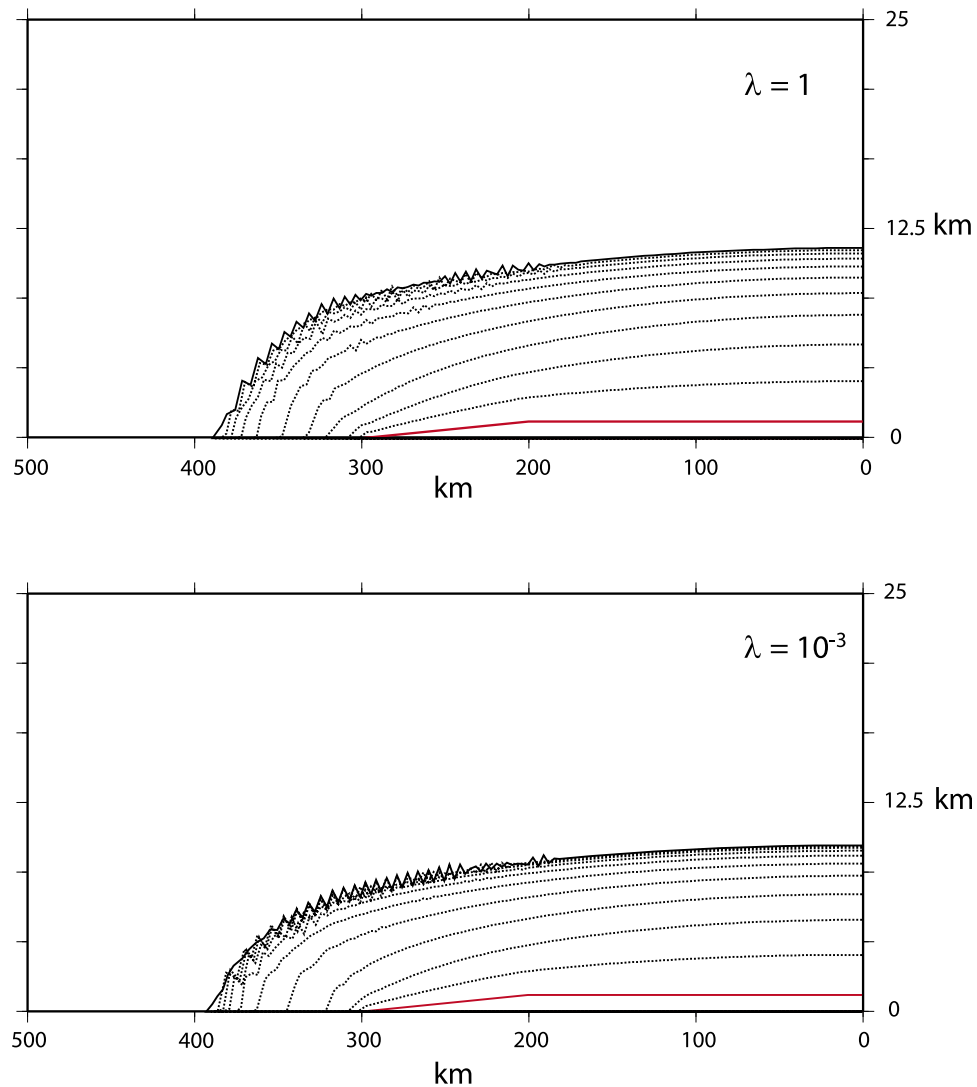


Figure 8. Plots of time-dependent solutions for the melt-solid interface. The top frame corresponds to $\lambda = 1$ and the bottom frame to $\lambda = 10^{-3}$. The red line represents the initial shape at $t = 0$. The remaining contours are evenly spaced at 5 second intervals. The vertical scale has been strongly exaggerated to emphasize differences between solutions. This accentuates small, transient, long-wavelength instabilities on the surface of the current (as previously described) that do not influence the dynamics; the current shape has a stable time average at long times.

source) is to increase spreading rate and melt layer thickness.

[56] Current estimates of water content in the transition zone are of order 0.2–0.3 wt% [Huang *et al.*, 2005; Medin *et al.*, 2007]. Our model would therefore predict a layer 7–10 km thick (Figure 9a) that does not extend much beyond the upwelling regions (Figure 9b).

[57] In Figure 9c, we compare our full dynamic calculations of melt layer extent (stars, left axis) to steady-state estimates based on balances of water and silicate fluxes (dashed line, after Leahy and Bercovici [2007]) and find good agreement, within uncertainty, in the determination of the nose position. The diamonds (right axis) show how melt layer thickness is a function of transition zone water content. Figure 9d shows how time to steady structure is a decreasing function of water content.

4.5. Effects of Mantle Viscosity

[58] While melt layer structure is sensitive to the viscosity ratio between the solid and the melt, the absolute value of the ambient mantle viscosity plays a pivotal role. This is because melt spreading depends on displacing ambient fluid and the relevant timescale for this process. Here, for a constant transition zone water content, $c_{wd} = 0.3$ wt%, and viscosity ratio, $\lambda = 10^{-3}$, we systematically vary the mantle viscosity between 10^{20} and 10^{23} Pa s (cases 1, 12–14).

[59] We find that both the steady state height and the time to reach steady structure depend strongly on mantle viscosity (Figure 10). In particular, an order of magnitude increase in mantle viscosity corresponds roughly to a doubling in the time to steady state and a doubling of melt layer thickness.

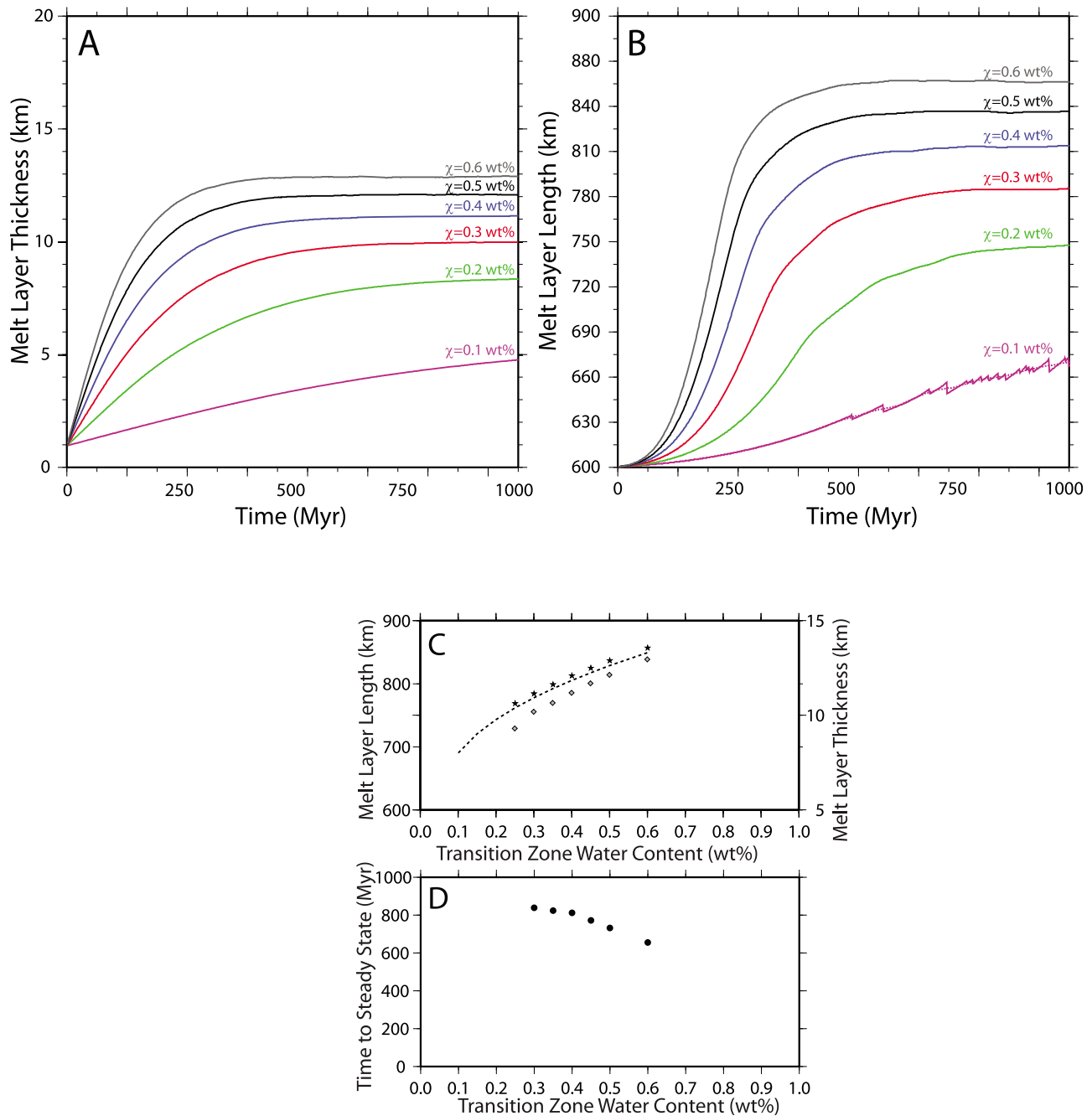


Figure 9. (a) Thickness of the melt layer versus time for increasing water content in the transition zone. (b) Length of the melt layer versus time for increasing water content. (c) Steady state melt layer length (left axis, stars) and time-independent melt layer thickness (right axis, diamonds) versus transition zone water content. The dashed line represents the steady-state extent derived from the mass balance calculation presented by Leahy and Bercovici [2007] and agrees with our result. (d) Time to steady structure versus mantle water content.

4.6. Effects of Temperature

[60] While our model includes no explicit temperature dependence, there are many places in which temperature may influence this process. In particular, temperature controls the ambient mantle viscosity (see the previous section). However, another more explicit effect is in determining the local equilibrium of the melting reaction. For all previous

calculations, we have considered a liquidus water content of $c_\ell = 15$ wt% [Litasov and Ohtani, 2002] and $c_s = 0.06$ wt% [Stalder et al., 2001], which are valid roughly around 1600°C. Using this and a dry melting point of 2000°C, we can construct a schematic phase diagram that allows us to systematically vary the ambient mantle temperature between 1600 and 1900 K (cases 1, 15–17).

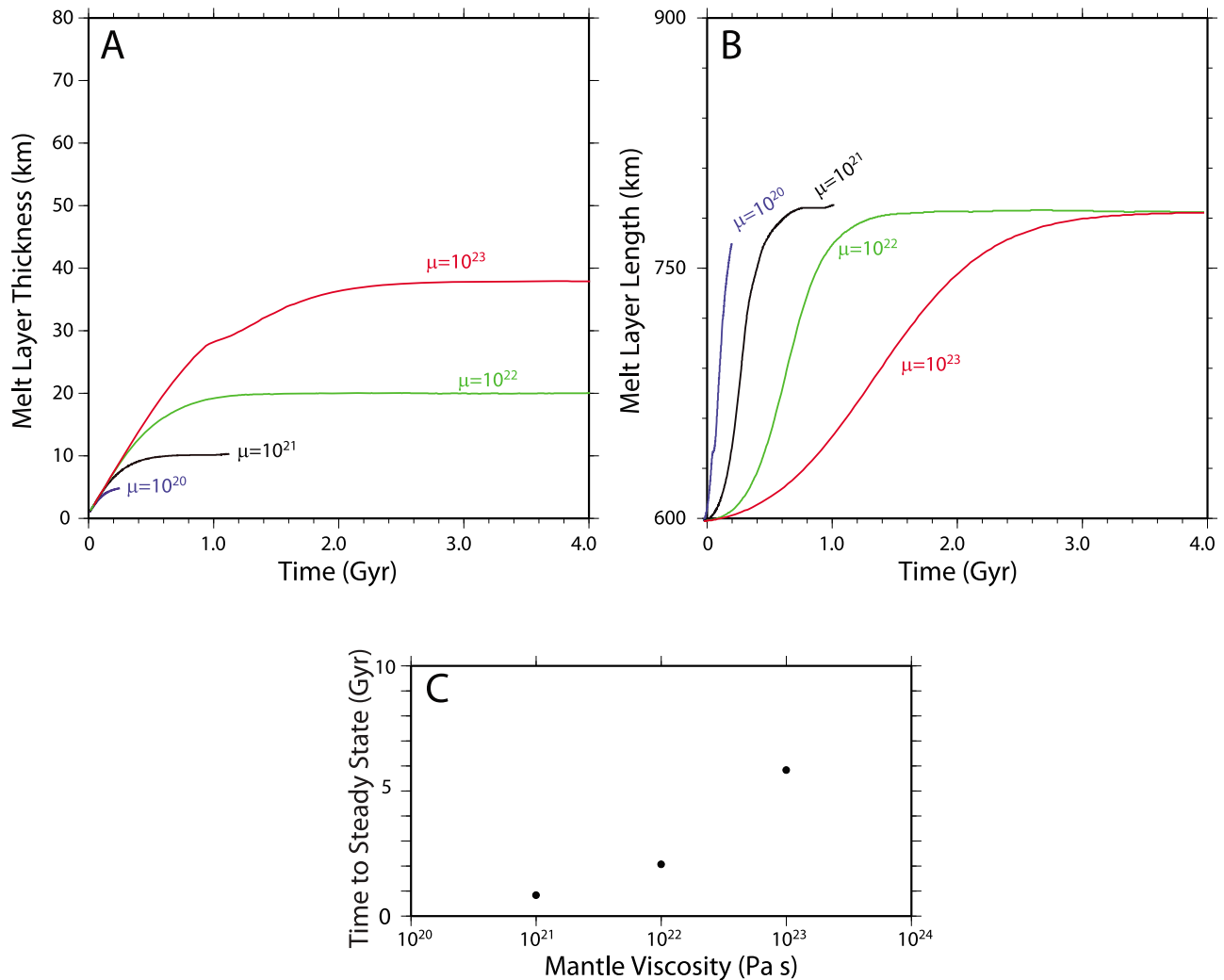


Figure 10. (a) Thickness of the melt layer versus time for increasing mantle viscosity. (b) Length of the melt layer versus time for increasing mantle viscosity. (c) Time to steady state versus mantle viscosity.

[61] The results of this calculation using $\lambda = 10^{-3}$, $\mu_{ol} = 10^{21}$ Pa s, and $c_{wd} = 0.3$ wt% are shown in Figure 11. Increasing the mantle temperature by 300°C leads to a thickening of the melt layer and a decrease in the time to steady state; this occurs because as temperature increases, both c_ℓ and c_s decrease, which raises the melt fraction and thereby increases the rate of the melt influx. Owing to poor constraints on the wadsleyite phase diagram, we have neglected how temperature affects water storage capacity in the transition zone.

5. Discussion

[62] In this study we have developed a self-consistent model for the evolution and structure of a dense hydrous melt layer above the transition zone. We have systematically explored several important parameters such as transition zone water content, mantle viscosity, melt/solid viscosity ratio, and temperature (Table 3). We find that a broad range of these parameters predict melt layer thicknesses that are of order 10–20 km and that reach steady state structures on plate tectonic timescales. *Bercovici and Karato* [2003]

predicted similar thicknesses, although their estimates were global averages.

[63] Though our model obtains similar melt layer extents to those predicted by *Leahy and Bercovici* [2007], it predicts significantly different melt layer thickness and shape. In the previous model, the melt layer achieves the classical gravity current shape, where the horizontal gradient in melt layer thickness drives flow within the current; as the current approaches the nose and the current thins, the horizontal gradient in thickness increases, reflecting increasing difficulty in driving flow through a narrow channel. The current shape and thickness is therefore the minimum thickness necessary to drive fluid flow to the nose, with the exact spatial gradients in current thickness required.

[64] In the current study, while flow through the melt layer must still accommodate the same magnitude sources and sinks, resistance to spreading is primarily in the outer fluid. The steady state shape obtained is not gravitationally stable, and we therefore propose it represents a dynamic equilibrium between viscous drag in the upper mantle and melt layer spreading; higher pressure (and therefore a thicker melt layer) is required to drive melt layer spreading.

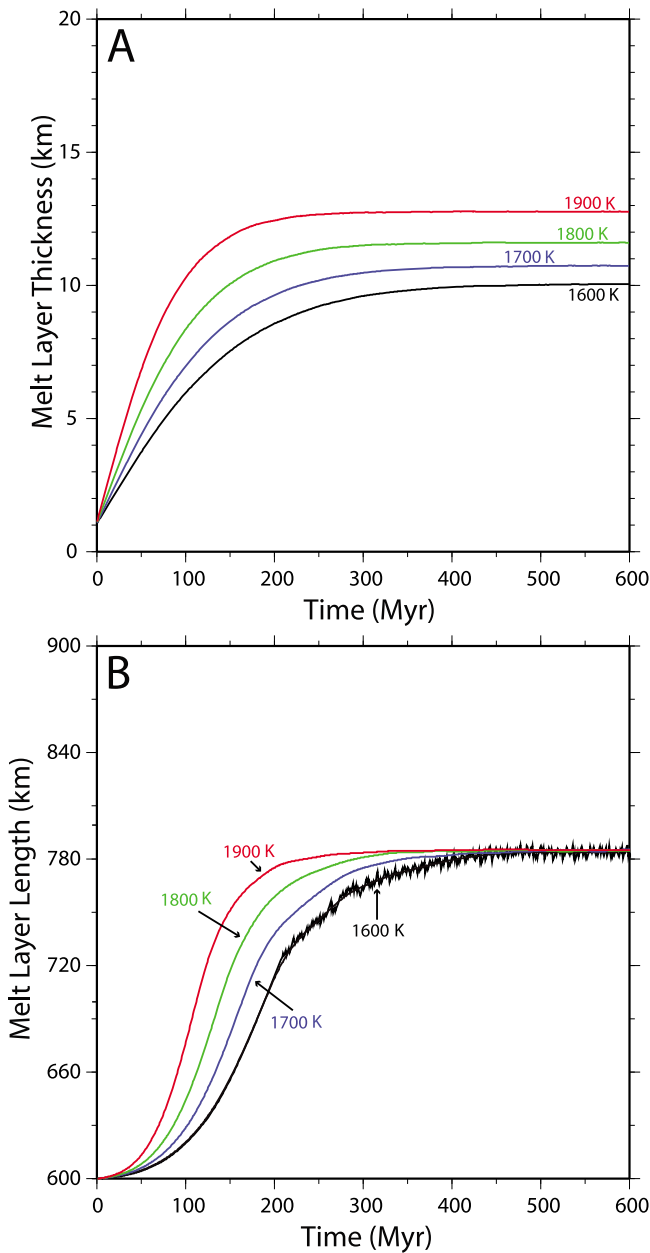


Figure 11. (a) Thickness of the melt layer versus time for increasing ambient mantle temperature. (b) Length of the melt layer versus time for increasing temperature.

[65] To test this hypothesis, we look to an analysis of the forces involved in the slender body limit. Following *Lister and Kerr* [1989], for a constant flux gravity current the height H , length L , and flux Q are related in the following manner:

$$HL = Qt \quad (30)$$

[66] The integrated gravitational force on the current F_b is

$$F_b \sim \int \frac{\partial P}{\partial x} dV \sim \int \Delta\rho g \frac{H}{L} dV = \Delta\rho g H^2 \quad (31)$$

in two dimensions, and the drag force on the current surface F_d is the integrated shear traction on the melt layer:

$$F_d \sim \frac{\mu L}{t} \quad (32)$$

in the limit that the current viscosity is small ($\lambda \rightarrow 0$). The exterior viscosity is μ and the thickness of the viscous boundary layer in the exterior fluid is assumed to scale as L (over which the stress is accommodated). By equating equations (31) and (32), and substituting $L = \frac{Qt}{H}$ from equation (30), we obtain

$$H = \sqrt[3]{\left(\frac{\mu Q}{\Delta\rho g}\right)} \quad (33)$$

[67] At large times, we apply this model to the shape of the current in the downwelling region. The flux $Q(x)$ at any position in the downwelling region is given by

$$Q(x) = \int_{x_0}^x S(x') dx' \quad (34)$$

where $S(x)$ is defined in equation (14) and x_0 is the center of the upwelling region. The resulting current shape from this simple analytic model correlates well with the full numerical solutions, as seen in Figure 12. Further, this model explains why the spreading time and structure is so sensitive to the viscosity of the outer medium and also why a steady state model that does not consider the exterior fluid would have significantly different structure.

[68] The detectability of a melt layer at 410 km remains an open question. A pure melt lens of 10–20 km thickness would certainly influence the interpretation of shear waves propagating through the mantle, depending on the melt's physical properties, and therefore should be easily recognized. However, the model discussed here neglects two-phase flow, particularly with regard to the decompaction rate of the melt layer.

[69] In a simple model, *Karato et al.* [2006] show that porosity in the melt layer is a strong function of rate of entrainment of the melt by downwelling mantle flow. Slow entrainment may allow the melt more time to segregate from the solid, especially if wetting is complete [*Yoshino et al.*, 2007]. Conversely, fast entrainment allows melt to remain in low porosity structures. However, *Karato et al.* [2006] neglect time dependence; our results suggest that in the initial phases of melt spreading the melt layer decompacts as melt accumulates (low entrainment rates). Initial decompaction could then directly affect the steady state structure. The effects of these processes on melt layer thickness are not directly evident; a better estimate of the interplay between porous structure and melt spreading is needed.

[70] This problem is further complicated by the fact that in downwelling regions, the melt is not in equilibrium with the matrix. This would add a phase change term to the compaction equations that may also act to increase porosity. We might therefore expect that even if the bulk of the upwelling region existed as a zone of accumulated partial melt, the entrainment regions may be marked by local areas of high porosity.

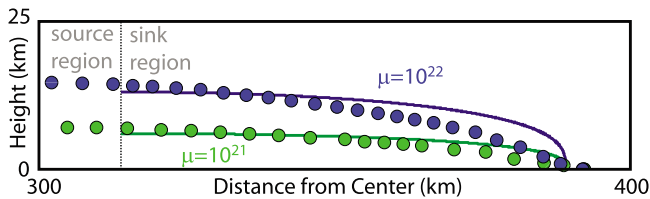


Figure 12. Here we take two solutions from our numerical model (circles) corresponding to solid mantle viscosities of $\mu = 10^{21}$ (green) and $\mu = 10^{22}$ (blue). For clarity we have shown only the nose of the current, which spans the downwelling region. The solid lines are calculated from equation (33) and compare favorably with our numerical calculations.

[71] Further, if the melt exists as a partial melt, this would reduce the influence of melt on shear wave structure. The exact effect of a partially molten system is not as simple as a proportional increase in thickness, as it depends on the entrainment and compaction rates [Karato *et al.*, 2006].

[72] Our results concerning the time evolution of the melt layer are particularly intriguing. We find that the typical timescales for achieving steady state structures are on the order of 500 Myr. This indicates that this mechanism may be nimble enough to adjust to changes in regional tectonic setting during supercontinent assembly or breakup while still efficiently recycling water back into the lower mantle.

[73] Of significant interest is the constraint that a 500 Myr timescale places on predictions of the geochemical signature resulting from the water filter mechanism. If incompatible elements were not recycled efficiently from the melt layer, the melt would be subject to zone refinement. The melt would accumulate trace elements until saturation, and its ability to filter upwelling mantle would be considerably reduced. However, as water is more compatible than most trace elements, it would likely reach equilibrium well in advance of other incompatible elements. Therefore, incompatible elements would continue to be stripped from the solid, and the water filter mechanism could act to deplete the mid-ocean ridge basalt source region throughout the lifetime of a typical ocean basin.

[74] While we find diffusive transport of water in the solid upper mantle to be negligible because it is slow relative to the melt layer spreading rate, several special cases remain in the parameter regime where diffusion could play a role. These are regions in which melt spreading is very slow relative to diffusion. This may be due to any combination of factors, including high mantle viscosity, low regional transition zone water content, small melt layer thickness, or relatively cool mantle temperatures (which would both suppress melting and increase the mantle viscosity).

[75] Slow spreading may be mitigated by the development of a water-rich boundary layer as in Figure 6 in solid mantle surrounding the melt lens. Several studies have shown that an order of magnitude increase in solid water content can lead to an order of magnitude increase in strain rate [e.g., Karato and Jung, 2003]. A water-rich boundary layer may therefore locally reduce the mantle viscosity by several orders of magnitude, which would correspond to an increase in spreading rate of a similar magnitude [Leahy, 2008].

[76] While our approach for obtaining models of melt layer structure is powerful and versatile, it has limitations. In

particular, the model would benefit from a comprehensive treatment of the effects of temperature, similar to the way we address the water budget and circulation. In such a scenario, additional terms representing latent heat fluxes upon melting and crystallization would be incorporated into the reaction equation, and we would more comprehensively model the effects of temperature on local equilibrium in a spatial and temporal sense. The inclusion of temperature dependence would also allow us to better model thermally induced topography on the phase transition; melt may accumulate in valleys, and the effective melt layer thickness (which governs spreading) would be determined relative to local peaks in topography.

[77] **Acknowledgments.** This work was supported under the NSF Graduate Research Fellowship and NSF grant EAR-0330745. We thank the editor and two anonymous reviewers for their thoughtful comments on the manuscript.

References

- Bercovici, D., and S. Karato (2003), Whole mantle convection and the transition-zone water filter, *Nature*, *425*, 39–44.
- Courtier, A. M., and J. Revenaugh (2007), Deep upper mantle melting beneath the Tasman and Coral Seas detected with ScS reverberations, *Earth Planet. Sci. Lett.*, *259*, 66–76.
- Fee, D., and K. Dueker (2004), Mantle transition zone topography and structure beneath the Yellowstone hotspot, *Geophys. Res. Lett.*, *31*, L18603, doi:10.1029/2004GL020636.
- Gao, W., S. Grand, W. Baldrige, D. Wilson, M. West, J. Ni, and R. Aster (2004), Upper mantle convection beneath the central Rio Grande rift imaged by P and S wave tomography, *J. Geophys. Res.*, *109*, B03305, doi:10.1029/2003JB002743.
- Gao, W., E. Matzel, and S. Grand (2006), Upper mantle seismic structure beneath eastern Mexico determined from P and S waveform inversion and its implications, *J. Geophys. Res.*, *111*, B08307, doi:10.1029/2006JB004304.
- Hirschmann, M., C. Aubaud, and A. Withers (2005), Storage capacity of H₂O in nominally anhydrous minerals in the upper mantle, *Earth Planet. Sci. Lett.*, *236*, 167–181.
- Huang, X., Y. Xu, and S. Karato (2005), Water content in the transition zone from electrical conductivity of wadsleyite and ringwoodite, *Nature*, *434*, 746–749.
- Illingworth, T. C., and I. O. Golosnoy (2005), Numerical solutions of diffusion-controlled moving boundary problems which conserve solute, *J. Comput. Phys.*, *209*, 207–225.
- Inoue, T. (1994), Effect of water on melting phase relations and melt composition in the system Mg₂SiO₄-MgSiO₃-H₂O up to 15GPa, *Phys. Earth Planet. Inter.*, *85*, 237–263.
- Jasbinsek, J., and K. Dueker (2007), Ubiquitous evidence for a low velocity layer atop the 410 km discontinuity, *Geochem. Geophys. Geosyst.*, *8*, Q10004, doi:10.1029/2007GC001661.
- Karato, S., and H. Jung (2003), Effects of pressure on high-temperature dislocation creep in olivine, *Philos. Mag.*, *83*, 404–414.
- Karato, S., D. Bercovici, G. M. Leahy, G. Richard, and Z. Jing (2006), The transition-zone water filter model for global material circulation: Where do we stand?, in *Earth's Deep Water Cycle*, *Geophys. Monogr. Ser.*, vol. 168, edited by S. Jacobsen and S. vander Lee, pp. 289–313, AGU, Washington, D. C.
- Koch, D., and D. Koch (1995), Numerical and theoretical solutions for a drop spreading below a free fluid surface, *J. Fluid Mech.*, *287*, 251–278.
- Leahy, G. M. (2008), Structure and dynamics of mid-mantle melt layers: Predictions and observations of hydrous melting above the transition zone, Ph.D. thesis, Yale Univ., New Haven, Conn.
- Leahy, G. M. (2009), Local variability in the 410-km mantle discontinuity under a hotspot, *Earth Planet. Sci. Lett.*, *288* (1–2), 158–163, doi:10.1016/j.epsl.2009.09.018.
- Leahy, G. M., and D. Bercovici (2007), On the dynamics of a hydrous melt layer above the transition zone, *J. Geophys. Res.*, *112*, B07401, doi:10.1029/2006JB004631.
- Lister, J. R., and R. C. Kerr (1989), The propagation of two-dimensional and axisymmetric viscous gravity currents at a fluid interface, *J. Fluid Mech.*, *203*, 215–249.

- Litasov, K., and E. Ohtani (2002), Phase relations and melt compositions in CMAS-pyrolite-H₂O system up to 25 GPa, *Phys. Earth Planet. Inter.*, 134, 105–127.
- Medin, A., R. Parker, and S. Constable (2007), Making sound inferences from geomagnetic sounding, *Phys. Earth Planet. Inter.*, 160(1), 51–59.
- Ohtani, E., H. Mizobata, and H. Yurimoto (2000), Stability of dense hydrous magnesium silicate phases in the system Mg₂SiO₄-H₂O and MgSiO₃-H₂O at pressures up to 27GPa, *Phys. Chem. Mineral.*, 27, 533–544.
- Pozrikidis, C. (1992), *Boundary Integral and Singularity Methods for Linearized Viscous Flows*, Cambridge Univ. Press, New York.
- Pozrikidis, C. (2001), Interfacial dynamics for Stokes flow, *J. Comput. Phys.*, 169, 250–301.
- Pozrikidis, C. (2002), *A Practical Guide to Boundary Integral Methods*, Chapman and Hall, London.
- Press, W. H., B. P. Flannery, S. A. Teukolsky, and W. T. Vetterling (1992), *Numerical Recipes in Fortran 77*, Cambridge Univ. Press, New York.
- Song, T., D. Helmberger, and S. Grand (2004), Low-velocity zone atop the 410-km seismic discontinuity in the northwestern United States, *Nature*, 427(6974), 530–533.
- Stalder, R., P. Ulmer, A. Thompson, and D. Günther (2001), High pressure fluids in the system MgO-SiO₂-H₂O under upper mantle conditions, *Contrib. Mineral. Petrol.*, 140, 607–618.
- Vinnik, L., and V. Farra (2002), Subcratonic low-velocity layer and flood basalts, *Geophys. Res. Lett.*, 29(4), 1049, doi:10.1029/2001GL014064.
- Yoshino, T., N. Yu, and S. Karato (2007), Complete wetting of olivine grain boundaries by a hydrous melt near the transition zone, *Earth Planet. Sci. Lett.*, 256, 466–472.
- Zener, C. (1949), Theory of growth of spherical precipitates from solid solution, *J. Appl. Phys.*, 20, 950–953.

D. Bercovici, Department of Geology and Geophysics, Yale University, New Haven, CT 06520, USA.

G. M. Leahy, Department of Geology and Geophysics, Woods Hole Oceanographic Institution, Mail Stop 24, Woods Hole, MA 02543, USA. (gleahy@whoi.edu)